Available online at www.sciencedirect.com
SCIENCE DIRECT®
Acta Materialia 53 (2005) 3765–3773
Acta MATERIALIA
www.actamat-journals.com

Shear band formation in columnar thermal barrier oxides

M. Watanabe *, T. Xu, C.G. Levi, A.S. Gandhi, A.G. Evans

Materials Department, University of California, Santa Barbara, CA 93106, USA

Received 22 January 2005; received in revised form 19 April 2005; accepted 19 April 2005
Available online 8 June 2005

Abstract

Columnar thermal barrier oxides either impressed or impacted by projectiles at high temperature develop kink bands. The bands emanate from sub-surface sites adjacent to the contact zone and extend diagonally toward the substrate. At the boundaries, the columns are cracked, indicating that the material has been weakened, and rendering them preferred sites for material removal upon subsequent impact. In some cases, the bands reach the interface with the thermally grown oxide and initiate a delamination crack. The experimental challenges in characterizing the bands and in relating their occurrence to constituent properties and microstructure are extreme. To address this limitation, the present article explores methods for numerical simulation of the bands. By modeling the material within the columns as a minimally porous Gurson solid and treating the inter-columnar material as a low density foam, it will be demonstrated that bands can be simulated consistent with those observed experimentally.

Keywords: Coating; Finite element analysis; Microindentation; High temperature deformation

1. Introduction

Thermal barrier materials for aero-engines are generally manufactured by using electron beam physical vapor deposition. Such materials have a columnar microstructure [1–7]. They respond to localized loads imposed at elevated temperature by the formation of shear bands (Fig. 1(a)) [8,9]. Similar bands have been observed in materials removed from engine airfoils, after engine exposure, caused by the impact of foreign objects (Fig. 1(c)) [10–14]. The severe plastic bending of the columns along the boundaries causes them to crack (Fig. 1(b)), weakening the material. The consequence is an accelerated rate of material removal during erosion. While the practical problem involves impact at velocities in the 300 m/s range [14], similar shear bands are found upon quasi-static impression at high temperature [8,9]. Accordingly, this method can be used as a characterization probe. One objective of this article is to examine the potential of this method to establish a protocol for calibrating a simulation model.

The experimental method requires a rigid substrate and sphere to confine the deformation to the thermal barrier layer in a manner analogous to that found in impacted coatings [8]. This is achieved by using alumina (or sapphire) substrates and spheres. The layer is deposited on the substrate at rates and rotations comparable to those used for actual airfoils, in order to generate a similar microstructure. The impression is conducted at temperatures relevant to turbine applications. While the method generates shear bands [8], it is arduous. It is thus unrealistic to expect the phenomenon to be adequately characterized solely by experimental means. Therefore, the primary intent of this article is to explore simulation approaches having the intrinsic ability to relate the mechanism to the salient constituent properties and microstructural features. The latter include the feathery morphology of individual column surfaces,

* Corresponding author. Present address: Materials Engineering Laboratory, Thermal Spray Group, National Institute for Materials Science, Tsukuba, Ibaraki 305-0047, Japan. Tel.: +81 298 592 469; fax: +81 298 592 401.
E-mail address: watanabe.makoto@nims.go.jp (M. Watanabe).

1359-6454/$30.00 © 2005 Acta Materialia Inc. Published by Elsevier Ltd. All rights reserved.
doi:10.1016/j.actamat.2005.04.029

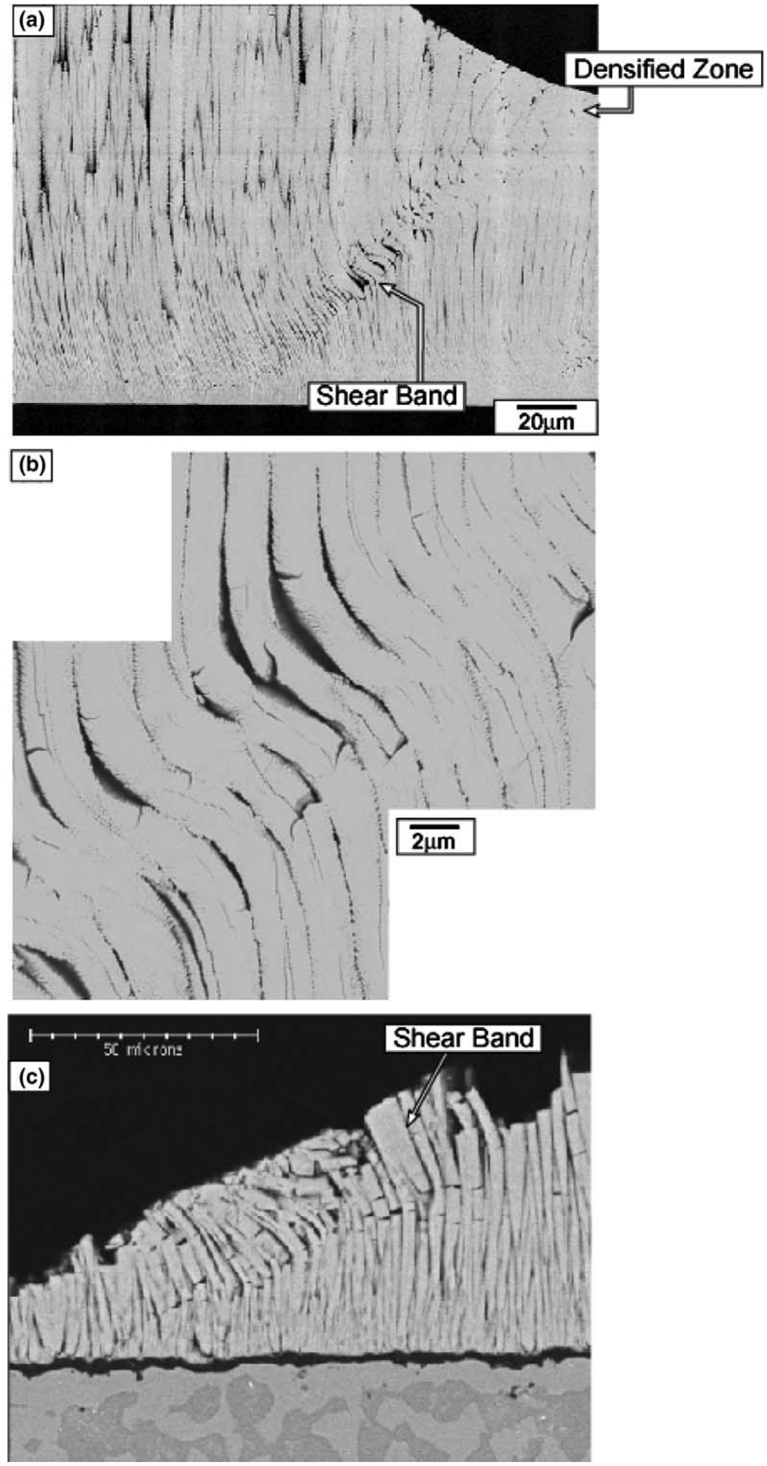

Fig. 1. Aspects of kink bands observed in 7YSZ: (a) a band induced by high temperature impression [8]; (b) a higher resolution image of the band shown in (a) highlighting the plastic bending, as well as the cracks at the boundaries and the separation between columns within the band; (c) a band found in an airfoil removed from an aero-engine showing a similar band, with the material above the band removed.

isolated pores inside the columns, and an inter-columnar zone (Fig. 2).

Since the shear bands appear to be intimately connected with the columnar microstructure (possibly analogous to kink bands found in fiber composites) [15,16], the preferred approach for numerical simulation is to include the microstructure explicitly, rather than relying on a constitutive law. The specific challenge relates to the constitutive laws to be used to characterize the slightly porous material comprising the columns and the highly porous material between the columns. Various concepts are explored. Once a viable simulation

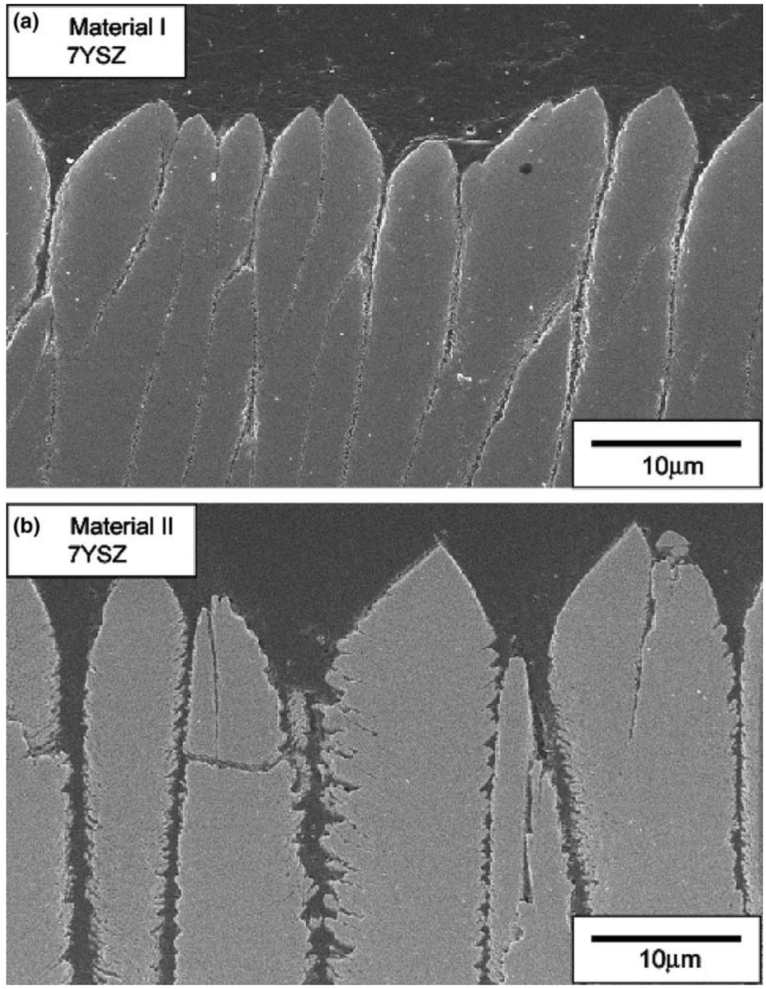

Fig. 2. The two microstructures investigated in the study: (a) material I (7YSZ) with a narrow inter-columnar zone; (b) material II with a wide inter-columnar zone (7YSZ). Material III is $Gd_2Zr_2O_7$ having the same microstructure as (a).

method has been identified, it will be used to characterize trends in the length and width of the bands as functions of microstructure and composition.

2. Measurements

2.1. Materials and procedures

The measurements have been conducted on three different materials (I, II and III) with the initial microstructures depicted in Fig. 2. Two of the materials have the same composition (7 wt.% yttria stabilized zirconia: 7YSZ) but different microstructures, in the sense that the inter-columnar zone, width b, is wider in material II (Fig. 2(b)) than in material I (Fig. 2(a)). Material III is $Gd_2Zr_2O_7$ with microstructure similar to material I (Fig. 2(a)). Materials I and III were deposited in the electron beam system at the University of California, Santa Barbara, while the material II was deposited by an industrial process. During deposition, the substrates were actively heated to 1000 °C and rotated around a horizontal axis above the source ingot. Evaporation was achieved with a 40 kV electron beam at ~6 kW, with an oxygen partial pressure of ~0.67 Pa. The oxide layer thickness was ~200 μm.

The tests were performed in air within a furnace located inside a servo-hydraulic test frame, which allows the loads to be measured as the spherical sapphire indenter (~500 μm diameter) penetrates. By using a displacement gage connected through the furnace to the loading platens, the associated displacement may also be estimated. After a plastic impression is created on the surface (Fig. 3(a)), sectioning through the center of that impression reveals the profile and allows determination of the plastic penetration (Fig. 3(b)). In all cases, the impressions are found to be spherical, indicating that they conform to the shape of the indenting sphere with minimal elastic recovery. Comparison of the final penetrations ascertained from the gage with those found from the cross-sections reveals a substantial discrepancy: the actual plastic penetrations are less than the gage displacements. This discrepancy arises even though the gage is in the hot zone close to the indenting sphere.

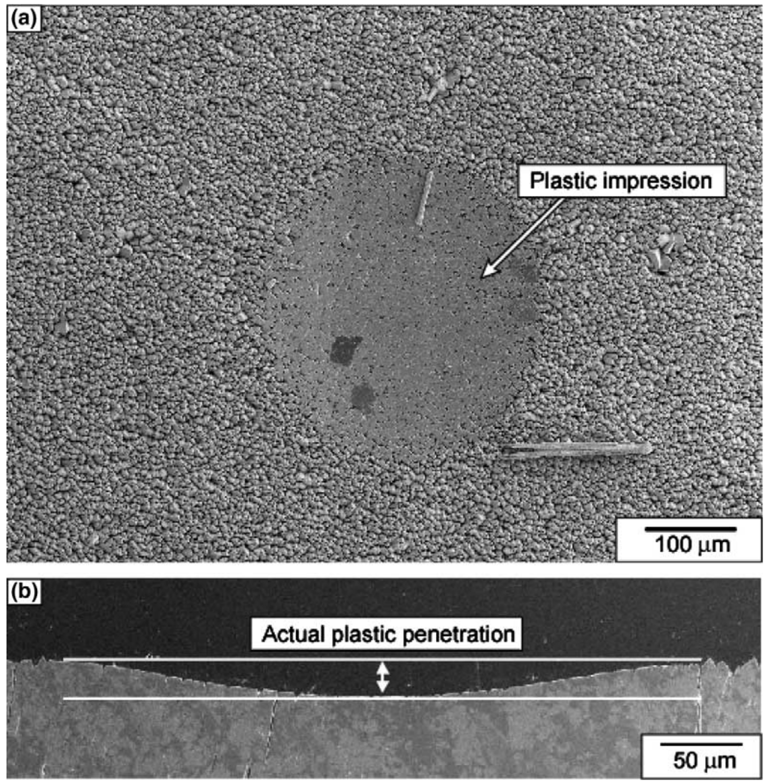

Fig. 3. (a) A plan view of a plastic impression created by a rigid sphere at 1150 °C. (b) A cross-section of the plastic impression in (a).

Accordingly, the load–displacement responses are revised using actual plastic penetrations. This is achieved by scaling the measured displacements to the penetration ascertained from the cross sections.

2.2. Results

Trends in load with penetration are plotted in Fig. 4(a). For a specified penetration, the 7YSZ with the narrower inter-columnar zone (material I) supports an appreciably larger load than material II with the same composition but more widely separated columns (Fig. 2). The corresponding load levels for material III (the $Gd_2Zr_2O_7$) are comparable to those for material I. The major implication is that the penetration loads are governed primarily by microstructure and are insensitive to composition. The penetration pressures, p (hardness), for materials I and II are plotted in Figs. 4(b) and (c) as a function of the plastic penetration, δ_{pl}. (These results should supplant those presented in an earlier publication [8].) They fit the linear relationship:

$$p = p_0(\delta_{pl}/h_{tbc}), \qquad (1)$$

where h_{tbc} is the thickness of the oxide layer and p_0 is a reference pressure (15 GPa for material I and 5 GPa for material II).

A range of the kink band patterns found in the experiments is presented in Fig. 5. As noted in a previous investigation [8], the bands are planar (not axisymmetric): they are normal to the plane having the largest inter-columnar zone width, as governed by the direction of rotation during deposition [1]. Consistent with previous observations [8], material II with the wide inter-columnar zone densifies beneath the impression and forms inclined bands between the dense and unaffected domains (Fig. 5(a)). Conversely, material I (as well as material III) exhibits multiple kink bands with minimal densification (Fig. 5(b)), except for that associated with the flattening of tops of the columns. Typically, the bands have inclinations relative to the vertical in the range, 35–45°. Generally, they appear to initiate sub-surface close to the center of the impression and extend downward. The bands are planar and align normal to the direction with the widest inter-columnar gaps (i.e., along the rotation axis). The bands have width, $w \approx 2d$, where d is the column width. They vary in length in a manner yet to be characterized. The cracks at the band boundaries partially penetrate the columns with appreciable opening displacements (Fig. 1(b)), indicative of accompanying plasticity. Within the bands, the columns separate as a consequence of their rotation.

3. Simulation methods

3.1. Strategy

A tractable approach for incorporating the microstructure has been sought by conducting numerous

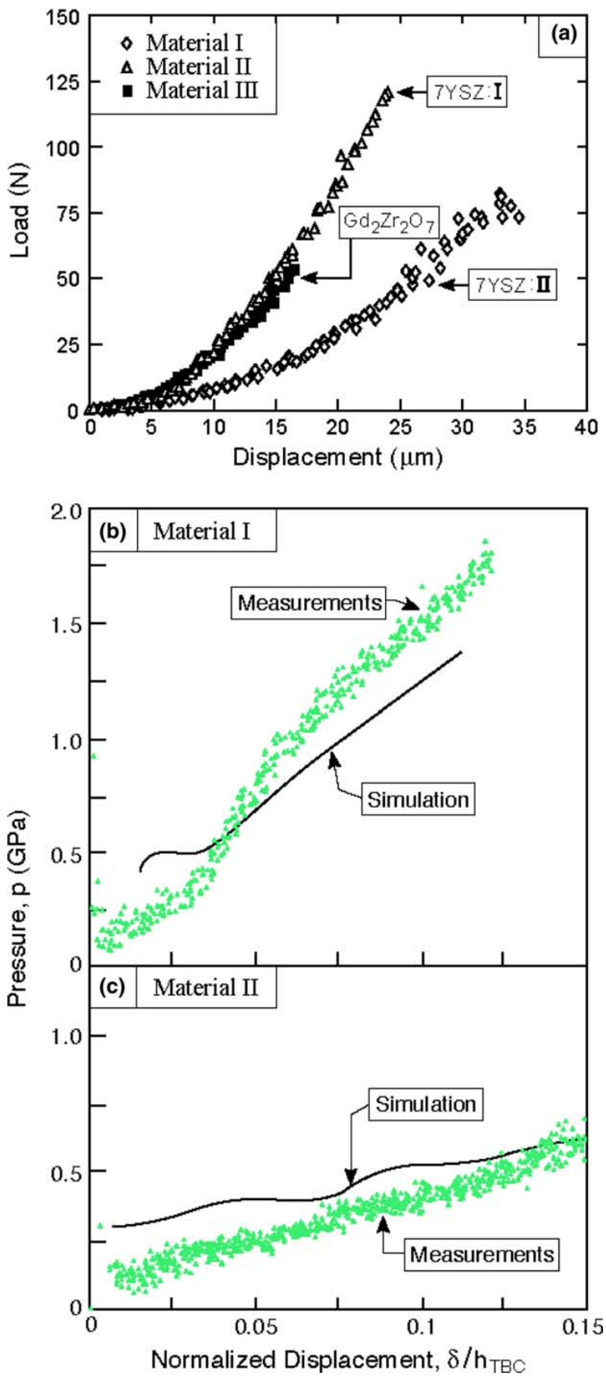

Fig. 4. Measurements obtained during sphere indentation at 1150 °C: (a) load as a function of plastic impression depth for all three materials; (b) the indentation pressure as a function of plastic penetration for the 7YSZ material I; (c) the indentation pressure as a function of plastic penetration for the 7YSZ material II. The lines in figures (b) and (c) are simulated results that, based on the present model, give the best fit to the data. These fits are used to calibrate the model.

preliminary calculations and by selecting the approach that rendered shear bands most closely resembling those found in the experiments. A full 3D model is not viable for the extensive calculations need to understand the mechanism. Among the 2D options, a plane strain (rather than axisymmetric) model appears to be preferable, possibly because the bands are planar [8]. The pressures deduced from the model can be connected to those obtained experimentally by using standard results from penetration mechanics [17]. To obtain column displacements similar to those found experimentally, sticking friction is invoked at the contact between the sphere and the surface [9]. The other key choice concerns the representation of the inter-columnar zone. Two possibilities have been considered.

(i) Following a previous study [9] the microstructure was modeled as discrete columns with gaps. Where the columns contact during impressing, the surfaces were assigned a friction coefficient. The variables are the column width, the gap width and the inter-columnar friction coefficient. This model has the evident disadvantage that the in-plane stiffness is zero.
(ii) Since there is a material between the columns (Fig. 2), as well as a finite in-plane tensile modulus [18], this zone is modeled as a highly porous medium using a constitutive law developed for metal foams [19]. This approach allows the known in-plane modulus to be matched. Moreover, since there is isolated porosity internal to the columns (of order 10%), the columns can be represented by a model for a minimally porous material, such as the Gurson solid [20].

The initial calculations have revealed that model (ii) provides a superior representation of the indentation pressures and the shear bands. This model is elaborated in the following section and used for the ensuing calculations presented in Section 4.

3.2. Numerical scheme

The columns are treated as elastic/perfectly plastic with isolated porosity. The yield strengths are obtained from measurements conducted on single crystals in the $\langle 100 \rangle$ orientation [21], representative of the texture developed during deposition [1]. The measurements are not at the same composition (10YSZ instead of 7YSZ). But since there are no data for 7YSZ, in order to proceed, we assume minimal composition dependence in this range. To incorporate the porosity, the Gurson law, which is available as an option in ABAQUS, is used. The potential is given as [20]:

$$\phi = \left(\frac{q}{\sigma_{\mathrm{Y}}}\right)^2 + 2q_1 f^* \cosh\left(q_2 \frac{\sigma}{2\sigma_{\mathrm{Y}}}\right) - (1 + q_3 f^{*2}) = 0, \tag{2}$$

where $q = \sqrt{(3/2)S:S}$ is the Mises equivalent stress and S is the deviatoric part of the Cauchy stress, σ. The yield strength of the fully dense material, σ_{Y}, is a function of $\varepsilon_{\mathrm{m}}^{\mathrm{pl}}$, the equivalent plastic strain. The void

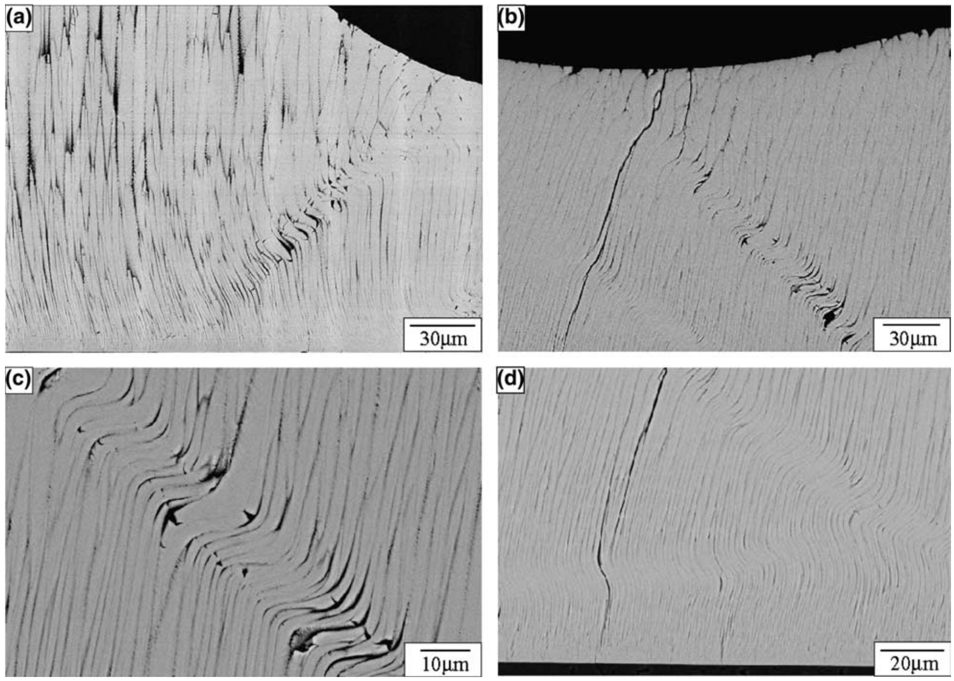

Fig. 5. Images of the range of different shear bands found in impression tests: (a) densified zone and shear band in material II (7YSZ with wide inter-columnar zone); (b) shear band without densified zone in material I (7YSZ with narrow inter-columnar zone); (c) magnified image of (b) showing the plastic bending that occurs within the kink band; (d) multiple kink bands found in material III ($Gd_2Zr_2O_7$ with narrow inter-columnar zone).

volume fraction term, f^* is related to the initial value, f_c, and that upon complete loss of load carrying capacity, f_F, by:

$$f^* = \begin{cases} f & \text{if } f \leqslant f_c, \\ f_c + \frac{\bar{f}_F - f_c}{f_F - f_c}(f - f_c) & \text{if } f_c < f < f_F, \\ \bar{f}_F & \text{if } f \geqslant f_F, \end{cases}$$

$$\text{where } \bar{f}_F = \frac{q_1 + \sqrt{q_1^2 - q_3}}{q_3}.$$

The unknown parameters, q_1, q_2, q_3, are calibrated in the following manner. The uniaxial yield strength of the dense solid is taken as the value measured for 10YSZ single crystals at 1150 °C [21], $\sigma_Y = 400$ MPa. With this choice, preliminary calculations are used to reveal that shear band formation is primarily affected by the choice of q_2. Consistency is achieved by using: $q_2 = 5$ and $q_1 = q_3 = 1$. Based on observations [1,22], the initial porosity is taken as: $f_c = 0.1$. The void fraction at load loss is assumed: $f_F = 0.9$. The Young's modulus $E = 200$ GPa and Poisson ratio $\nu = 0.25$ are adopted in all cases.

The *inter-columnar zone* has relatively low volume fraction of solid, comprising dendritic features with necks connecting adjacent columns (Fig. 3). This topology is reminiscent of open cell foams [19]. Accordingly, a foam model [19,20], which is also an option in ABAQUS, has been implemented. The crushable foam model has an elliptical yield surface

$$\left[\left(\frac{p_t - p_c}{2} + p\right)^2 + \left(\frac{q}{M}\right)^2\right]^{1/2} - \frac{p_c + p_t}{2} = 0, \tag{3}$$

where p_t is the yield strength of the material in hydrostatic tension and $p_c(\varepsilon_{vol}^{pl})$ the corresponding strength in hydrostatic compression (as a function of volumetric plastic strain). The quantity,

$$M = \sigma_0 \Big/ \sqrt{p_t p_{c0} - \frac{1}{3}\sigma_0(p_t - p_{c0}) - \frac{1}{9}(\sigma_0)^2}, \tag{4}$$

is the slope of the p–q plane that defines the axes of the elliptical surface: where σ_0 is the initial yield strength in uniaxial compression; and p_{c0} is the initial value of p_c. The protocol used to calibrate the model is described in the ensuing section.

4. Simulation results

The calculations are all performed using a TBC thickness of 200 μm, comparable to that for the samples used to perform the indentations. Two values of the inter-columnar zone width have been chosen to represent the microstructures shown in Fig. 2. For this purpose, the inter-columnar zone is considered to include the domain of "feathery" porosity along the sides of the columns: whereupon, $b/d = 1/16$ and $1/2$ for materials I/III and II, respectively (with b referring to the gap width between columns). It is not possible to conduct independent measurements of the unknown parameters that characterize the inter-columnar zone. They are selected on the basis of comparisons with the measurements of the indentation pressure (Fig. 4) and of the shear band patterns (Fig. 5). Initial calculations reveal that the intra-column porosity and the yield strength of the material in this zone are the two most important parameters affecting the indentation pressure and the incidence of shear bands. To obtain a consistent best fit to the pressure data, this comparison (Figs. 4(b) and (c)) indicates that the tensile stress at yield is, $\sigma_0 \approx 20$ MPa and remains invariant through the indentation. However, due to densification, the compressive strength must be allowed to vary from the same initial value ($\sigma_0 \approx 20$ MPa) to the yield strength of the dense solid ($\sigma_0 = 400$ MPa) when the volumetric plastic strain reaches unity. This procedure incorporates the increase in indentation pressure with penetration (Fig. 4). Unless indicated otherwise, these choices are used for all ensuing calculations.

Typical deformation pattern, with associated kink bands, are presented in Figs. 6 and 7. All the results in Fig. 6 are for an intra-columnar porosity of 10%. Those in Fig. 7 are for a corresponding porosity of 2%. The results in Figs. 6(a) and (b) refer to material II with the wider inter-columnar zone ($b/d = 1/2$). Those in Figs. 6(c) and 7 are for materials I/III with a narrower

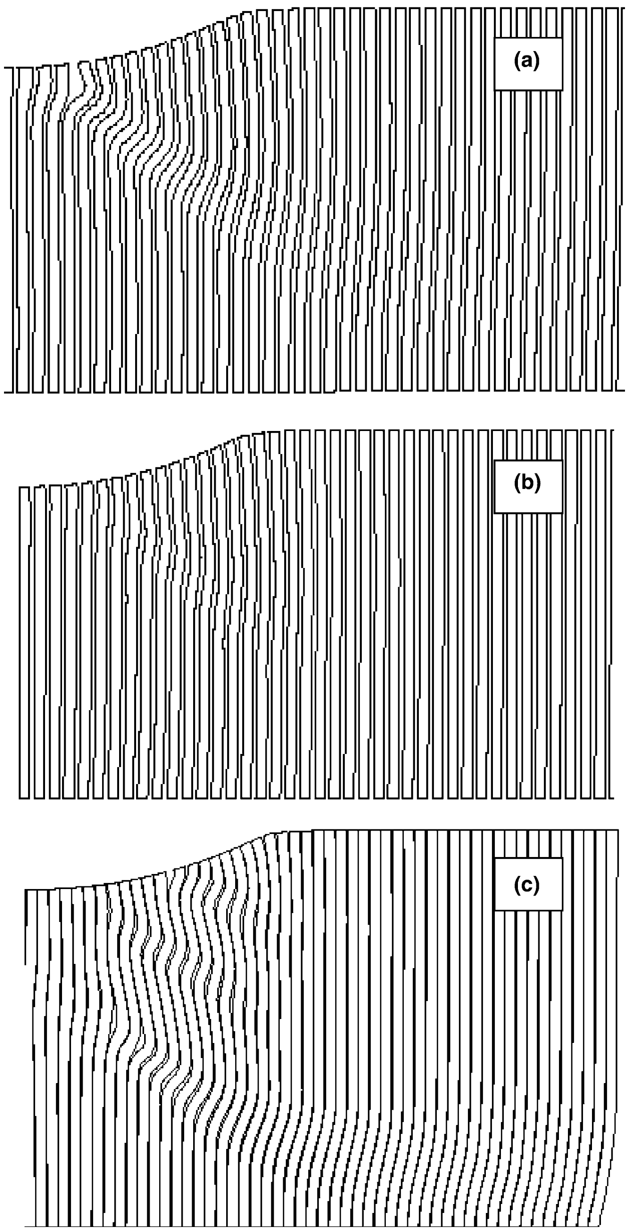

Fig. 6. Various shear bands obtained by simulation. All are for an initial intra-columnar porosity of 10%: (a) microstructure comparable to material II, with inter-columnar width, $b/d = 1/2$ and the following parameters: intra-columnar yield strength, $\sigma_0 = 400$ MPa, initial inter-columnar strength, 20 MPa (in tension and compression) with compressive strength increasing to 400 MPa at a strain of unity; (b) same as (a) except that the initial strength of the inter-columnar zone has been increased to 40 MPa. Note that this change suppresses the shear bands; (c) microstructure comparable to materials I and III with inter-columnar zone width, $b/d = 1/6$: otherwise the properties are the same as (a).

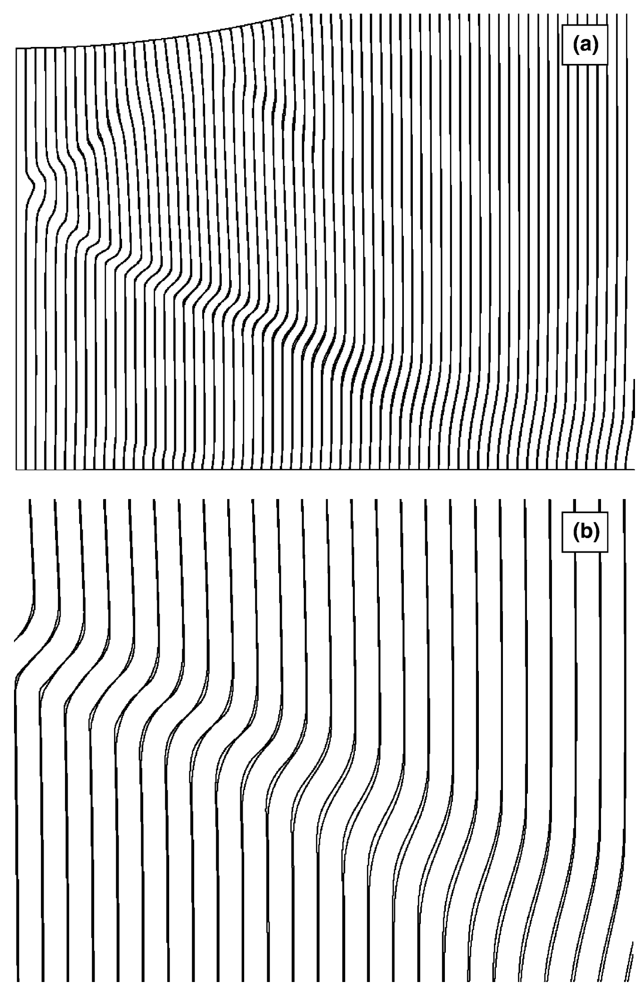

Fig. 7. Simulated shear bands for microstructure I or III with inter-columnar zone width, $b/d = 1/6$, assuming an initial intra-columnar porosity of 2%: (a) overview and (b) magnified view of the opening between columns within the band.

inter-columnar zone, $b/d = 1/6$. Note that the deformation pattern for material II becomes relatively homogeneous and the bands are eliminated (Fig. 6(b)) when the inter-columnar material has somewhat higher strength than that needed to fit the indentation pressure results in Fig. 4 (i.e., 40 MPa instead of 20 MPa). For material I, multiple bands are formed (Figs. 6(c) and 7), but the pattern changes as the intra-columnar porosity changes from 10% (Fig. 6(c)) to 2% (Fig. 7). The correspondence between these simulated responses and the observed behaviors summarized in Fig. 5 provide affirmation of the utility of the current modeling approach.

The lengths and widths of the bands have been ascertained as a function of the impression depth (Fig. 8) for the models most representative of materials I and II. The principal features are as follows. The bands only form when the impression depth exceeds a threshold, δ_{th}. Thereafter, the band length, ℓ, increases linearly with increase in impression depth. They can be fit by the approximate relationship

$$\ell \approx \ell_0[\delta_{pl} - \delta_{th}]/h_{tbc}, \tag{5}$$

where the length scale $\ell_0 = 1.7$ and 3 mm for materials I and II, respectively. The corresponding thresholds are: $\delta_{th}/h_{tbc} = 0.07, 0.04$. Upon initiation, the bands are narrow, but increase in width as they become fully developed, with asymptote $w \approx 2d$. The latter is consistent with the observations (Fig. 1).

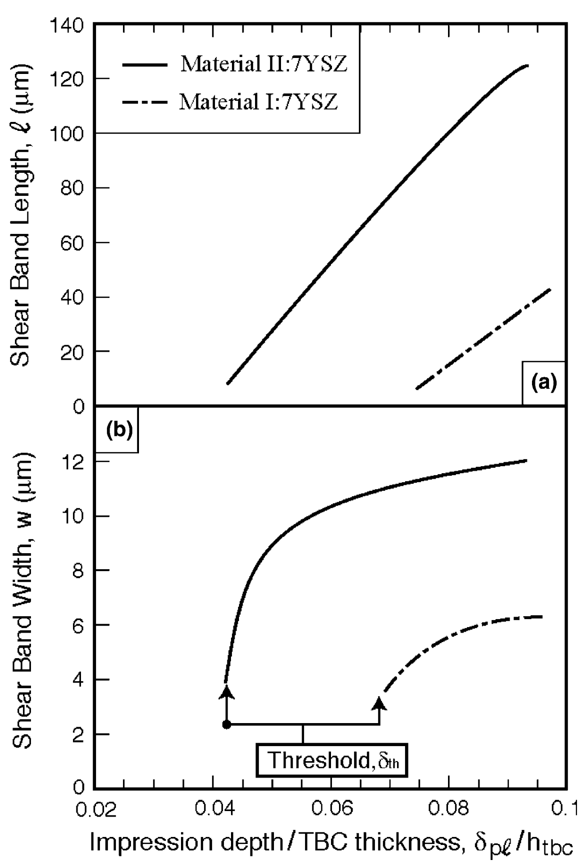

Fig. 8. Calculations of the trends in (a) shear band length and (b) band width as a function of the impression depth for materials I and II.

5. Implications

A combination of Figs. 4 and 8 provides the basis for predicting the lengths and widths of shear bands created by the impact of hard projectiles. To ascertain this information, we note that the plastic work done by a spherical projectile (radius R, density ρ and velocity v), as it penetrates is [17]: $W_{pl} = \pi p R \delta_{pl}^2$. This work counteracts the kinetic energy of the projectile: $W_{pl} = \frac{2}{3}\pi R^3 v^2 \rho$. Accordingly, the plastic penetration is related to the velocity by

$$\left(\frac{\delta_{pl}}{R}\right)^2 = \frac{3}{2}\left[\frac{v^2\rho}{p}\right]. \tag{6a}$$

Incorporating p from (1) gives

$$\left(\frac{\delta_{pl}}{h_{tbc}}\right)^3 = \frac{2}{3}\left[\frac{v^2\rho}{p_0}\right]\left(\frac{R}{h_{tbc}}\right)^2. \tag{6b}$$

The shear band length is then obtained from (5) as:

$$\frac{\ell}{\ell_0} = \sqrt[3]{\frac{2}{3}\frac{v^2\rho}{p_0}\left(\frac{R}{h_{tbc}}\right)^2} - \frac{\delta_{th}}{h_{tbc}}. \tag{6c}$$

By letting, $\ell = 0$, the threshold velocity below which there should be no shear bands becomes

$$v_{th} = \left(\frac{\delta_{th}}{h_{tbc}}\right)^{3/2}\frac{h_{tbc}}{R}\sqrt{\frac{3}{2}\frac{p_0}{\rho}}. \tag{6d}$$

The critical velocity at which the shear band extends through the TBC layer to create a delamination is obtained by equating ℓ to h_{tbc}, giving

$$v_c = \left[\frac{h_{tbc}}{\ell_0} + \frac{\delta_{th}}{h_{tbc}}\right]^{3/2}\frac{h_{tbc}}{R}\sqrt{\frac{3}{2}\frac{p_0}{\rho}}. \tag{6e}$$

By assuming that the particles have the density of silica, $\rho = 2.5 \times 10^6$ g/m^3, that $h_{tbc} = 100$ μm and that the particles have radius, $R = 50$ μm, the threshold velocities for materials I and II are 110 and 30 m/s, respectively. Recall that these apply when the TBC is at 1150 °C. Larger threshold velocities are expected at lower temperatures [8]. The corresponding critical velocities are, 300 and 70 m/s, respectively.

6. Conclusion

Measurements and observations of shear bands that form in columnar thermal barrier oxides when impressed or impacted by hard particles have been used to motivate the development of a simulation procedure. The measurements indicate a strong influence of microstructure on the deformation loads as well as on the propensity for shear band formation. The composition appears to exert a much smaller influence. The microstructural observations suggest that the material be regarded as two disparate materials: an intra-columnar zone with minimal isolated porosity adjoined by a highly porous inter-columnar zone. Preliminary finite element calculations have indicated that the former may be modeled as a Gurson solid, while the latter can be incorporated into a finite element scheme by invoking a response characteristic of that found for foams. The unknown constituent properties for the inter-columnar zone are calibrated by overlaying simulations of the indentation pressures with experimental measurements.

Once calibrated, the model has been used to demonstrate shear band features that closely resemble those found experimentally. Moreover, the development of the bands as the projectiles penetrate has been predicted for two different microstructures. The results have been used to define two characteristic impact velocities: one representing the threshold for shear band formation and the other a critical velocity above which the bands propagate to the interface and induce delaminations.

References

[1] Levi CG. Curr Opin Solid State Mater Sci 2004;8:77.
[2] Evans AG, Mumm DR, Hutchinson JW, Meier GH, Pettit FS. Prog Mater Sci 2001;46:505.
[3] Padture N, Gell M, Jordan E. Science 2002;296:280.
[4] Stiger MJ, Yanar NM, Toppings MG, Pettit FS, Meier GH. Z Metallknd 1999;90:1069.
[5] Ruud JA, Bartz A, Borom MP, Johnson CA. J Am Ceram Soc 2001;84:1545.
[6] Mumm DR, Evans AG, Spitsberg IT. Acta Mater 2001;49:1793.
[7] Clarke DR, Levi CG. Ann Rev Mater Sci 2003;33:383.
[8] Watanabe M, Mercer C, Levi CG, Evans AG. Acta Mater 2004;52:1479.
[9] Chen X, Hutchinson JW, Evans AG. Acta Mater 2004;52:565.
[10] Chen X, Wang R, Yao N, Evans AG, Hutchinson JW, Bruce RW. Mater Sci Eng 2003;A352:221.
[11] Chen X, He MY, Spitsberg IT, Fleck NA, Hutchinson JW, Evans AG. Wear 2004;256:735.
[12] Nicholls JR, Deakin MJ, Rickerby DS. Wear 1999;23:352.
[13] Wellman RG, Nicholls JR. Wear 2000;89:242.
[14] Bruce RW. Trib Trans 1998;41:399.
[15] Budiansky B, Fleck NA. J Mech Phys Solids 1993;41:183.
[16] Fleck NA, Deng L, Budiansky B. J Appl Mech 1995;62:329.
[17] Johnson KL. Contact mechanics. Cambridge: Cambridge University Press; 1985.
[18] Johnson CA, Ruud JA, Bruce R, Wortman D. Surf Coat Technol 1998;108:80.
[19] Deshpande VS, Fleck NA. J Mech Phys Solids 2000;48:1253.
[20] ABAQUS version 5.8 User's Manual, Pawtucket, RI: Hibbit, Karlsson & Sorensen Inc; 1998.
[21] Messerschmidt U, Baither D, Baufeld B, Bartsch M. Mater Sci Eng 1997;A233:61.
[22] Kulkarni AA, Herman H, Almer J, Lienert U, Haeffner D. J Am Ceram Soc 2004;87:268.